University of Groningen

The Evolution of the Broadband Temporal Features Observed in the Black-hole Transient MAXI J1820+070 with Insight-HXMT

Wang, Yanan; Ji, Long; Zhang, S.; Méndez, Mariano; Qu, J. L.; Maggi, Pierre; Ge, M. Y.; Qiao, Erlin; Tao, L.; Zhang, S.

IMPORTANT NOTE: You are advised to consult the publisher's version (publisher's PDF) if you wish to cite from it. Please check the document version below.

Document Version
Publisher's PDF, also known as Version of record

Publication date:
2020

Link to publication in University of Groningen/UMCG research database

The Evolution of the Broadband Temporal Features Observed in the Black-hole Transient MAXI J1820+070 with Insight-HXMT

Yanan Wang[1], Long Ji[2], S. N. Zhang[3,4], Mariano Méndez[5], J. L. Qu[3,4], Pierre Maggi[1], M. Y. Ge[3], Erlin Qiao[6], L. Tao[3], S. Zhang[3], Diego Altamirano[7], L. Zhang[7], X. Ma[3], F. J. Lu[3], T. P. Li[3,4,8], Y. Huang[3], S. J. Zheng[3], Y. P. Chen[3], Z. Chang[3], Y. L. Tuo[3,4], C. Güngör[3,9], L. M. Song[3,4], Y. P. Xu[3], X. L. Cao[3], Y. Chen[3], C. Z. Liu[3], Q. C. Bu[3], C. Cai[3], G. Chen[3], L. Chen[10], T. X. Chen[3], Y. B. Chen[8], W. Cui[8], W. W. Cui[3], J. K. Deng[8], Y. W. Dong[3], Y. Y. Du[3], M. X. Fu[8], G. H. Gao[3,4], H. Gao[3,4], M. Gao[3], Y. D. Gu[3], J. Guan[3], C. C. Guo[3,4], D. W. Han[3], J. Huo[3], S. M. Jia[3], L. H. Jiang[3], W. C. Jiang[3], J. Jin[3], Y. J. Jin[10], L. D. Kong[3,4], B. Li[3], C. K. Li[3], G. Li[3], M. S. Li[3], W. Li[3], X. Li[3], X. B. Li[3], X. F. Li[3], Y. G. Li[3], Z. W. Li[3], X. H. Liang[3], J. Y. Liao[3], G. Q. Liu[8], H. W. Liu[3], X. J. Liu[3], Y. N. Liu[8], B. Lu[3], X. F. Lu[3], Q. Luo[3,4], T. Luo[3], B. Meng[3], Y. Nang[3,4], J. Y. Nie[3], G. Ou[3], N. Sai[3,4], R. C. Shang[8], X. Y. Song[3], L. Sun[3], Y. Tan[3], G. F. Wang[3], J. Wang[3], W. S. Wang[3], Y. D. Wang[11], Y. S. Wang[3], X. Y. Wen[3], B. B. Wu[3], B. Y. Wu[3,4], M. Wu[3], G. C. Xiao[3,4], S. Xiao[3,4], S. L. Xiong[3], J. W. Yang[3], S. Yang[3], Y. J. Yang[3], Y. J. Yang[3], Q. B. Yi[3,4], Q. Q. Yin[3], Y. You[3], A. M. Zhang[3], C. M. Zhang[3], F. Zhang[3], H. M. Zhang[3], J. Zhang[3], T. Zhang[3], W. C. Zhang[3], W. Zhang[3,4], W. Z. Zhang[10], Y. Zhang[3], Y. F. Zhang[3], Y. J. Zhang[3], Y. Zhang[3,4], Z. Zhang[8], Z. Zhang[8], Z. L. Zhang[3], H. S. Zhao[3], X. F. Zhao[3,4], D. K. Zhou[3,4], J. F. Zhou[8], R. L. Zhuang[10], Y. X. Zhu[3], Y. Zhu[3], and Lingjun Wang[3]

[1] Université de Strasbourg, CNRS, Observatoire astronomique de Strasbourg, UMR 7550, F-67000 Strasbourg, France; yanan.wang@astro.unistra.fr
[2] Institut für Astronomie und Astrophysik, Kepler Center for Astro and Particle Physics, Eberhard Karls Universität, Sand 1, D-72076 Tübingen, Germany
[3] Key Laboratory for Particle Astrophysics, Institute of High Energy Physics, Chinese Academy of Sciences, 19B Yuquan Road, Beijing 100049, People's Republic of China
[4] University of Chinese Academy of Sciences, Chinese Academy of Sciences, Beijing 100049, People's Republic of China
[5] Kapteyn Astronomical Institute, University of Groningen, P.O. Box 800, 9700 AV Groningen, The Netherlands
[6] Key Laboratory of Space Astronomy and Technology, National Astronomical Observatories, Chinese Academy of Sciences, Beijing 100101, People's Republic of China
[7] Physics & Astronomy, University of Southampton, Southampton, Hampshire SO17 1BJ, UK
[8] Department of Astronomy, Tsinghua University, Beijing 100084, People's Republic of China
[9] Istanbul University, Science Faculty, Department of Astronomy and Space Sciences, Beyazıt, 34119, Istanbul, Turkey
[10] Department of Engineering Physics, Tsinghua University, Beijing 100084, People's Republic of China
[11] Department of Astronomy, Beijing Normal University, Beijing 100088, People's Republic of China

Abstract

We study the evolution of the temporal properties of MAXI J1820+070 during the 2018 outburst in its hard state from MJD 58,190 to 58,289 with Insight-HXMT in a broad energy band 1–150 keV. We find different behaviors of the hardness ratio, the fractional rms and time lag before and after MJD 58,257, suggesting a transition occurred around this point. The observed time lags between the soft photons in the 1–5 keV band and the hard photons in higher energy bands, up to 150 keV, are frequency-dependent: the time lags in the low-frequency range, 2–10 mHz, are both soft and hard lags with a timescale of dozens of seconds but without a clear trend along the outburst; the time lags in the high-frequency range, 1–10 Hz, are only hard lags with a timescale of tens of milliseconds; they first increase until around MJD 58,257 and decrease after this date. The high-frequency time lags are significantly correlated to the photon index derived from the fit to the quasi-simultaneous NICER spectrum in the 1–10 keV band. This result is qualitatively consistent with a model in which the high-frequency time lags are produced by Comptonization in a jet.

Unified Astronomy Thesaurus concepts: Black holes (162); Compact objects (288); Low-mass x-ray binary stars (939)

1. Introduction

X-ray variability is present in accreting black holes (BHs) on timescales of milliseconds to years: for example, flares (Belloni et al. 2000; Altamirano et al. 2011), quasi-periodic oscillations (QPOs; van der Klis 1989), dips (Kuulkers et al. 1998; Kajava et al. 2019), and broadband noise (Méndez & van der Klis 1997; Takizawa et al. 1997; Casella et al. 2005; Motta et al. 2015). The variability associated with source spectral state reveals not only the mass accretion rate but also the geometry and structure of the system. Understanding the variability is crucial both to understanding the accretion process and to determining the source properties (Uttley et al. 2014).

Another important measurement of the variability is the time lag between soft and hard photons (e.g., Nowak et al. 1999;

Altamirano & Méndez 2015; Zhang et al. 2017). The timescale of time lags reflects the underlying physical process that produces the variability and the evolution of the lags along the outburst may also reveal the changes of the geometry of the system. Hard lags (hard photons lag the soft ones) correlated with the shape of the spectral continuum up to around 30 keV in the hard state have been reported in several systems, e.g., Cyg X-1 (Pottschmidt et al. 2003; Grinberg et al. 2014) and GX 339–4 (Nowak et al. 2002; Altamirano & Méndez 2015). Reig et al. (2018) analyzed this correlated behavior in 12 outbursts of eight BH systems and confirm the photon-index-time-lag correlation as a global property of BH X-ray binaries.

Additionally, three main canonical states driven by the mass accretion rate have been widely used to describe a full outburst in BH transients: hard, soft, and intermediate states, identified

by their timing and spectral properties (Tanaka & Lewin 1995; van der Klis 1995; Méndez et al. 1997; Remillard & McClintock 2006). Each state shows timing and spectral complex characteristics; hardness, defined as the ratio between count rates in different bands, has been demonstrated as a useful parameter to understand the spectral evolution of outbursts. However, one sometimes failed to finish a transition loop; for the transients that do not enter a soft state, this type of outburst has been dubbed a "failed" outburst, e.g., H 1743–322 (Capitanio et al. 2009; Zhou et al. 2013) and Swift J1753.5–0127 (Soleri et al. 2013). Capitanio et al. (2009) proposed that the case during the 2008 outburst of H 1743–322 was associated with a premature decrease of the mass accretion rate.

The BH candidate (BHC) MAXI J1820+070 was discovered on 2018 March 11 in X-rays with the Monitor of All-sky X-ray Image (MAXI; Matsuoka et al. 2009). After four days, the Hard X-ray Modulation Telescope (HXMT), dubbed Insight-HXMT, started obtaining observations, which extended until 2018 October. MAXI J1820 is a bright source with a luminosity of up to 10^{37} erg s^{-1} in the energy band 0.01–100 keV (Shidatsu et al. 2019), assuming a distance of 3 kpc (Gandhi et al. 2018). This nearby luminous X-ray source, brighter than 4 Crab in 15–50 keV, makes itself an ideal target for Insight-HXMT. Recently, Torres et al. (2019) confirmed MAXI J1820 to be a BH transient with a dynamical mass measurement, constraining the BH mass to be 7–8 $M_\odot$ when the inclination angle is 69°–77°. Later on, Atri et al. (2019) refined the mass of the BH in MAXI J1820 to be $9.5 \pm 1.4\ M_\odot$ by measuring the distance to the source with the Very Long Baseline Array and the European Very Long Baseline Interferometry Network.

Kara et al. (2019) conducted a spectral and timing analysis to study the geometry of the hard emission region in MAXI J1820. By observing the changes of the reverberation lags between 0.1–1.0 and 1.0–10.0 keV energy photons, they suggest that the corona shrinks vertically as the source evolves from the hard toward the soft state. Meanwhile, the accretion disk shows no evolution along the outburst. Both findings have been supported by the work done by Buisson et al. (2019) in which they analyzed some Nuclear Spectroscopic Telescope Array (Harrison et al. 2013) observations, covering the period of the data used in Kara et al. (2019).

In this paper, we carry out a detailed time- and Fourier-domain analysis of MAXI J1820 using Insight-HXMT data, together with the spectral analysis using NICER data, to investigate the X-ray variability observed in the luminous hard state.

2. Observations and Data Reduction

Insight-HXMT was launched on 2017 June 15. It carries three slat-collimated instruments on board (Zhang et al. 2020), the High Energy X-ray telescope (HE: 20–250 keV; Liu et al. 2020), the Medium Energy X-ray telescope (ME: 5–30 keV; Cao et al. 2020; Guo et al. 2020) and the Low Energy X-ray telescope (LE: 1–15 keV; Chen et al. 2020; Liao et al. 2020).

The entire outburst of MAXI J1820 has been observed with Insight-HXMT between 2018 March and October. Owing to the broad energy band and high time resolution (LE: 1 ms; ME: 280 μs; HE: 25 μs) of Insight-HXMT, we performed a statistical analysis of the X-ray timing properties of MAXI J1820, up to 150 keV, of 63 observations from MJD 58,197 to 58,288, in the
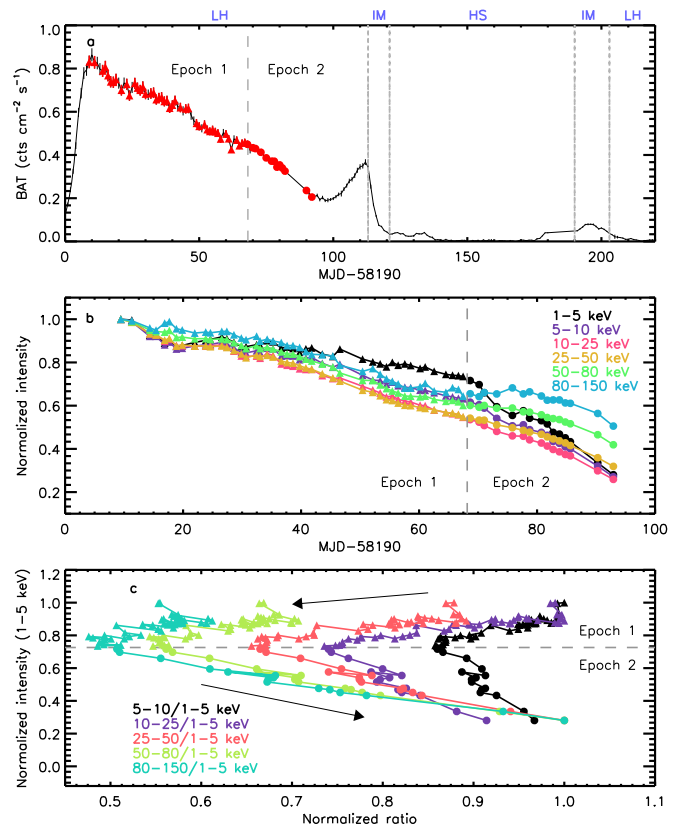
Figure 1. Panel (a): The Swift/BAT light curve of MAXI J1820 in the 15–50 keV band during the 2018 outburst. The red triangles and circles, corresponding to epochs 1 and 2 (here and in the following figures), respectively, indicate the simultaneous Insight-HXMT observations used in this paper. The gray dotted lines indicate the states of the source, taken from Shidatsu et al. (2019). "LH," "IM," and "HS" are short for low hard, intermediate, and high soft state, respectively. Panel (b): The normalized HXMT light curves in different energy bands. Panel (c): the normalized HID in different energy bands, evolving from the top right to the left and back to the bottom right as indicated by the arrows. The black, purple, orange, green, and cyan symbols indicate the hardness ratio between, respectively, the energy bands 5–10, 10–25, 25–50, 50–80, and 80–150 keV, with respect to the 1–5 keV band.

hard state of the outburst (see the definition of the spectral states in Shidatsu et al. 2019). In Figure 1, we show the 15–50 keV long-term SWIFT/BAT light curve with the indication of the spectral states of MAXI J1820. The red triangles and circles in panel (a) correspond to the simultaneous observational time of Insight-HXMT.

We extracted the data from all three instruments using the Insight-HXMT Data Analysis software (HXMTDAS) v2.00.[12] We created the good-time-intervals based on the suggested criteria: (1) the offset for the pointing position is ⩽0°.05; (2) the Earth elevation angle is >6°; (3) the geomagnetic cutoff rigidity is >6°; (4) the extraction time is at least 300 s before or after the South Atlantic Anomaly passage. To avoid possible contamination from the bright Earth and nearby sources, we applied the small field of view for all the detectors (Chen et al. 2018; Huang et al. 2018).

We conducted spectral analysis with NICER in the 1–10 keV of MAXI J1820. We chose NICER over Insight-HXMT because NICER has a larger effective area than Insight-HXMT in this energy band. The data processing and filtering was

---

[12] http://enghxmt.ihep.ac.cn/fxrj.jhtml

performed using HEASoft 6.26.1 and NICERDAS version 6. We followed standard data reduction steps to run the filtering, calibration, and merging of NICER events. We excluded two of the active FPMs 14 and 34, which are often found to exhibit episodes of increased detector noise. After data had been cleaned and calibrated, we extracted the NICER spectra using XSELECT. The background is estimated with the tool, NIBACKGEN3C50.

3. Results

The evolution of the BAT light curve in Figure 1(a) shows that the intensity of MAXI J1820 increased rapidly by a factor of ∼7 and reached the peak of the outburst at ∼0.85 BAT counts s^{-1} cm^{-2} within the first 11 days, from MJD 58,190 to 58,210. In the following 90 days the intensity slowly decreased to around 0.2 BAT counts s^{-1} cm^{-2}. However, the intensity of MAXI J1820 increased again on MJD 58,288 and then reached a peak two times fainter than the previous one. At around MJD 58,306 the outburst reached a local minimum of the intensity.

We generated the Insight-HXMT light curves in the 1–5, 5–10, 10–25, 25–50, 50–80, and 80–150 keV energy bands to see how the X-ray emission in different energy bands changes in the luminous hard state. We then computed hardness ratios using the 1–5 keV light curve as the reference. We show the normalized light curves and hardness–intensity diagrams in Figure 1 in which we divided the intensity and the hardness ratio by their maximum values in each energy band for the purpose of display. Figure 1(b) shows that the intensity in all energy bands decreases with time; the intensity in the softest band, 1–5 keV, shows the slowest decrease before MJD 58,257 and the fastest decrease after MJD 58,257. Figure 1(c) shows that the hardness ratio first decreases along the outburst, reaching a local minimum at around MJD 58,246, then remains constant for a while and finally increases from MJD 58,257. The evolution of the HIDs suggests a transition at MJD 58,257. We therefore separated the data set into two groups, epochs 1 and 2, before and after the transition point. The triangles and circles represent, respectively, epochs 1 and 2 in all figures in this work.

3.1. X-Ray Variability in Time- and Fourier-domain

Figure 2(a) shows part of the 1–10 keV light curve of the BH transient MAXI J1820 at MJD 58,210. Similar to some other accreting BHs (e.g., GX 339–4 and XTE J1550–564), the light curve of MAXI J1820 shows various flares, which appear as peaked broadband noise in the Fourier power density spectrum (PDS). To explore this further, we created power spectra with stingray,[13] a software for timing analysis of X-ray data (Huppenkothen et al. 2019): for this, we divided the data into continuous 500 s segments with a time bin of 0.005 s, computed periodograms for each segment and averaged all periodograms in each observation.

Figure 2(b) shows the corresponding power spectrum at MJD 58,210 with Leahy normalization in the frequency range 0.002–100 Hz in different energy bands, while the power remains constant at around 2 at frequencies above 100 Hz. We thus subtracted the Poisson noise level of 2 to calculate the fractional rms. The power spectra in the 1–5 keV and 5–10 keV

[13] https://github.com/StingraySoftware/stingray
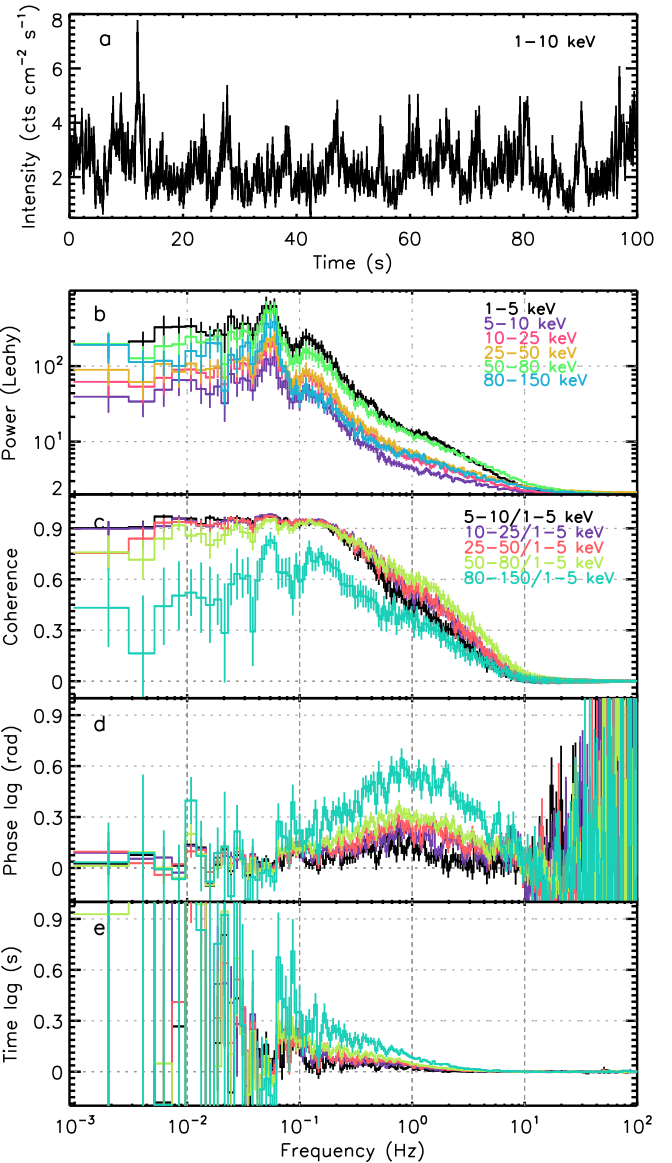
Figure 2. From top to bottom: the power spectrum, raw coherence, phase lags, and time lags in different energy bands of MAXI J1820 at MJD 58,210.

bands, respectively, show the highest and lowest power; the power spectra in other energy bands rank in between those two. Each of power spectrum can be described by a combination of several Lorentzians and a power law, displaying broadband noise plus a low-frequency QPO with a centroid frequency at 0.054 Hz. The QPO centroid frequency in different energy bands shows no significant shift. A second peak in the PDS is potentially a harmonic of the 0.054 Hz QPO, although data with higher signal-to-noise would be required to confirm this.

The centroid frequency of the detected QPOs in the observations used in this work ranges between 0.04 and 0.56 Hz; the QPO frequency first increases with time in epoch 1 and then decreases with time in epoch 2. More details of the QPO information will be presented in X. Ma et al. (2020, in preparation). As we aim to study the properties of the broadband noise, we computed the fractional rms in the low-frequency range, 2–10 mHz, below the QPO centroid frequency, and in the high-frequency range, 1–10 Hz, above
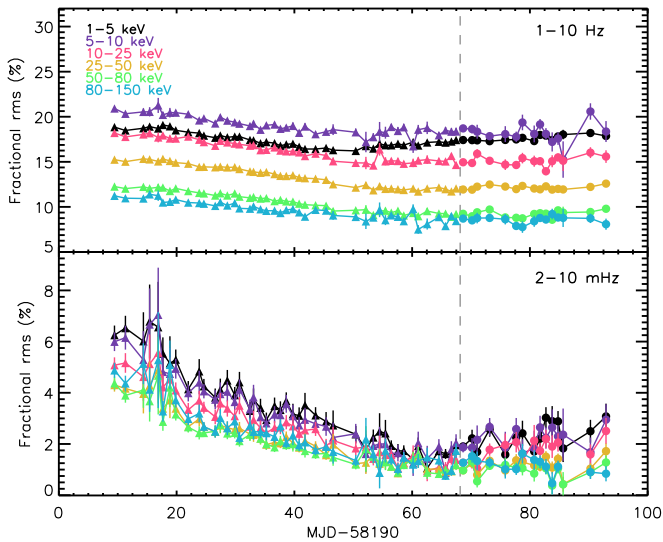
Figure 3. Frequency-dependent fractional rms amplitude of the broadband noise in MAXI J1820 in different energy bands.

Figure 4. Frequency-dependent time lag of the broadband noise in MAXI J1820 between the 1–5 and the 5–10, 10–25, 25–50, 50–80, and 80–150 keV bands as a function of time.

the QPO centroid frequency, one measurement per observation. We show the fractional rms as a function of time in Figure 3.

As shown in Figure 3, the high-frequency fractional rms amplitude is larger than the low-frequency one in the same energy band; the former slightly decreases along the outburst until MJD 58,240 in epoch 1 and after that remains more or less constant; the latter shows a similar behavior to the former but with larger uncertainties, it decreases much more dramatically with time in epoch 1, and then increases with volatility in epoch 2 except for the rms at energies above 25 keV. The difference between the same energy bands of the former is larger than that of the latter. These results are consistent with the fact that the low-frequency part of the PDS changes more significantly than the high-frequency part along the outburst.

The largest fractional rms amplitude in the 1–10 Hz frequency range is in the 5–10 keV band, followed by the rms in the other energy bands, suggesting a significant contribution of the reflection component to the variability. Excepting that band, the fractional rms amplitude in all other energy bands, both in the low-frequency and high-frequency ranges, decreases with increasing energy.

3.2. Frequency-dependent Time Lag

We computed the time lag between soft and hard photons (Nowak et al. 1999) to constrain models and emission geometry. We first used stingray to create cross-spectra of each selected observation of MAXI J1820 between the soft X-rays in the 1–5 keV band and the hard X-rays in the 5–10 keV, 10–25 keV, 25–50 keV, 50–80 keV, and 80–150 keV bands, respectively. We illustrate the raw coherence, phase-lag, and time-lag spectra in Figures 2(c), (d), and (e). The mean count rate for each band is 751.1, 146.4, 316.2, 1440.0, 651.9, and 364.5 cts s^{-1}, respectively.

There are two local peaks in each coherence spectrum at the QPO fundamental and suspected harmonic frequencies in the power spectra; both peaks become more significant with increasing energy (see Figure 2(c)). Figures 2(d) and (e) show that both the phase- and time-lag spectra below the QPO frequency are noisy; a dip appears at around the QPO frequency, 0.054 Hz, and the lags immediately increase after that. Meanwhile the time lags are correlated with energy, being larger at higher
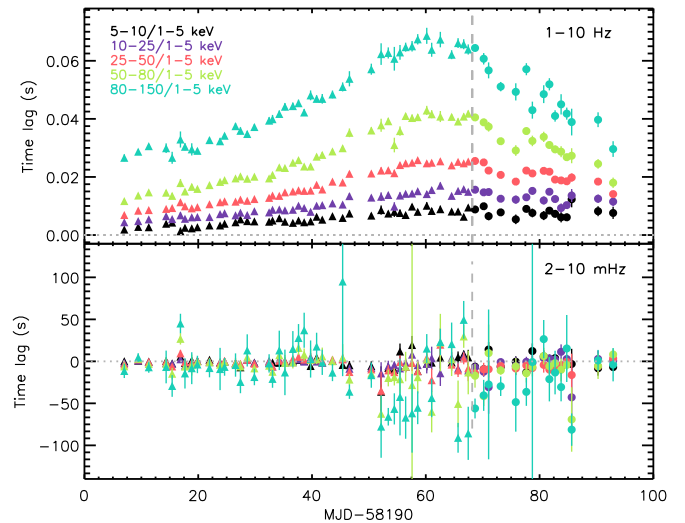
energies. We show a few examples of the time lag versus energy, together with their power spectra, in Figure A1 in which we use the average photon energy for each energy band.

To study the evolution of the frequency-dependent time lags along the outburst, we calculated the time lags in the 2–10 mHz and 1–10 Hz frequency ranges per observation. We first averaged the cross-spectrum over the 2–10 mHz and 1–10 Hz frequency ranges, respectively, and then calculated the time lags from the resulting phase lags of the averaged cross-spectrum. As shown in the upper panel of Figure 4, the high-frequency time lags increase with energy; the time lags increase with time in epoch 1 and decrease with time in epoch 2, except that the one in the 1–5 keV band is more or less constant; a dip is present at MJD 58,265 in all curves. The low-frequency time lags, shown in the lower panel of Figure 4, are significantly larger than the high-frequency lags and show both positive and negative values but without a clear trend with time.

3.3. Evolution of the Spectral Parameters

Figure 1 shows that the soft and hard parts of the spectrum evolve differently in epochs 1 and 2: the hard part of the spectrum drops more steeply than the soft part in epoch 1 whereas the soft part drops more steeply than the hard part in epoch 2, opposite to epoch 1; those changes result in a decreased hardness ratio in epoch 1 and an increased hardness ratio in epoch 2. To trace the energy-dependent changes of the intensity, we studied the NICER spectra of MAXI J1820 in the period of MJD 58,198–58,286 with exposure time longer than 1 ks. We analyzed the NICER spectra with the response matrix version 1.01 and the effective area file version 1.02.[14]

We fit each spectrum in the band 1–10 keV with a three component model consisting of a hard component for the persistent emission (POWERLAW in XSPEC), a multitemperature disk blackbody for the soft thermal emission (DISKBB in XSPEC) and a line model for the broad Fe emission line (GAUSSIAN in XSPEC). To account for the interstellar absorption, in all fits we used the component TBABS with solar abundances from Wilms et al. (2000) and photoelectric absorption cross-sections from

---

[14] https://heasarc.gsfc.nasa.gov/docs/nicer/proposals/nicer_tools.html
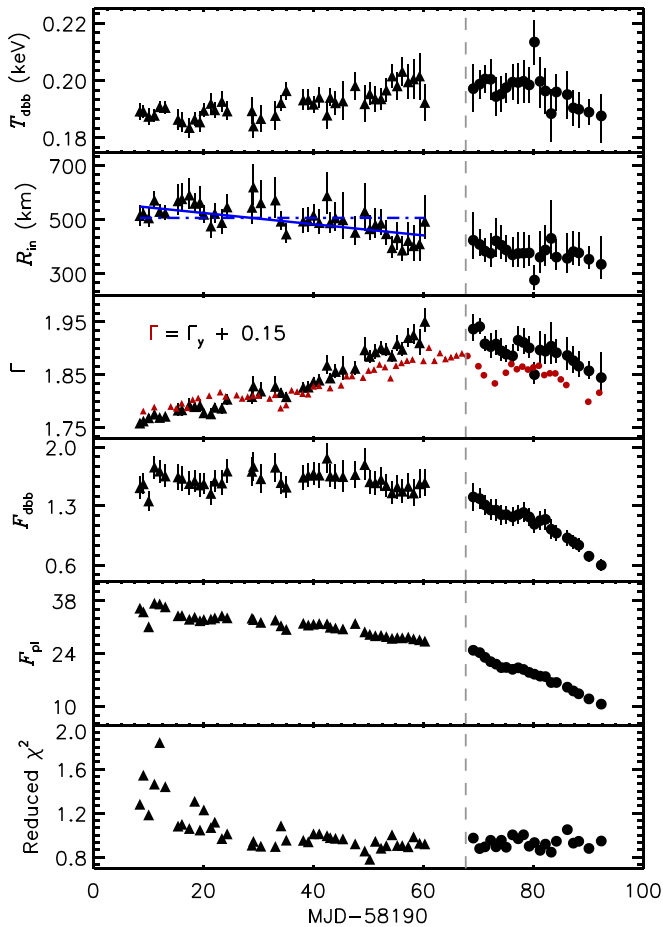
Figure 5. Best-fitting parameters of the NICER spectra of MAXI J1820. From top to bottom, the panels show, respectively, the evolution of the blackbody temperature, the inner radius of the accretion disk, the photon index, the DISKBB flux, the POWERLAW flux and the corresponding reduced χ^2. F_{dbb} and F_{pl} are in units of 10^{-9} erg s^{-1} cm^{-2}. The blue dashed–dotted and solid lines separately represent the constant and linear fit to the R_{in}–MJD relation in epoch 1. The photon index values plotted in red are from the paper of B. You et al. (2020, in preparation, see more details in Section. 3.3).

Verner et al. (1996). The overall model is TBABS∗(DISKBB +GAUSSIAN+POWERLAW).

Still, we found significant residuals at 2–3 keV, which are likely instrumental due to Au. We applied Crab correction to the spectra as described in Ludlam et al. (2018), whereas the residuals are still visible. We therefore ignored the energy band from 1.8 to 3 keV and added 0.5% systemic error to the fit to minimize the instrumental effect. The spectra, before MJD 58,290, require a narrow Fe emission line centered at 6.4–6.5 keV. Since either including this narrow line or not shows no significant effect on the best-fitting parameters of the continuum, we do not include this component in the fit. We quote errors at the 90% confidence level for the spectral analysis.

We show the temperature and the inner radius of the accretion disk, the power-law photon index and the reduced χ^2 as a function of time in Figure 5. The inner radius is derived from the DISKBB normalization, which is defined as $(R_{in}/D_{10})^2 * \cos\theta$, where R_{in} is the inner disk radius in kilometers, D_{10} is the distance to the source in units of 10 kpc, and θ is the disk inclination angle. We assumed $D_{10} = 0.3$ (Gandhi et al. 2018) and $\theta = 70°$ (Torres et al. 2019) in this work. Both the disk temperature and the photon index increase, whereas the inner disk radius decreases in epoch 1, indicating
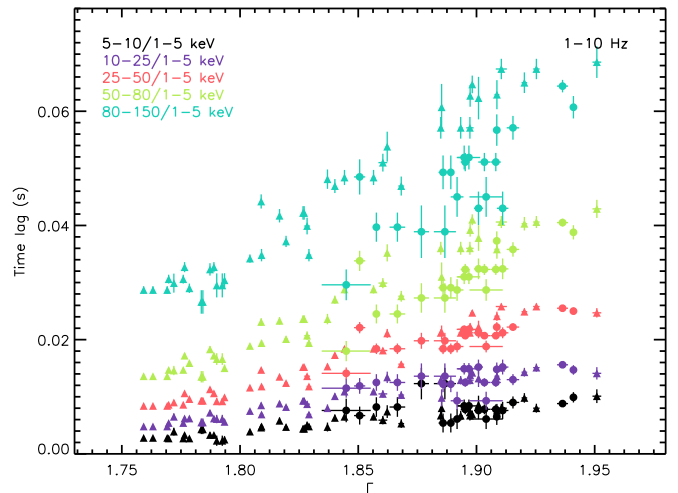
Figure 6. High-frequency time lags as a function of the photon index of the hard spectral component in MAXI J1820. As in Figure 1, the triangles and circles correspond to epochs 1 and 2, respectively.

that the source softens in this period. We fitted the evolution of the inner disk radius with both a constant and a decreasing linear function and got a better fit with the latter one, with associated F-test probability $\sim 9 \times 10^{-8}$, indicating that the evolution of inner disk radius in epoch 1 decreased with time.

However, the source did not enter the soft state, and instead became harder in epoch 2: the disk temperature and the photon index decreased even though the inner disk radius remained constant. The flux of the DISKBB component remains the same in epoch 1 when the flux of the POWERLAW component decreases by $\sim 30\%$; the fluxes of both the DISKBB and the POWERLAW components drop more than 50% in epoch 2. We plot the high-frequency time lags versus the photon index in Figure 6 and find that these two quantities are significantly correlated in all selected energy bands. The slopes of the lag–Γ relation in epochs 1 and 2 are consistent with each other except for the ones in the highest energy.

To test how much the assumption we made for the fit affects our result, we compare our best-fitting values of the photon index to the values taken from B. You et al. (2020, in preparation), since photon index is the only common parameter both in their and our work. They fit 199 Insight-HXMT spectra from 3 to 150 keV with the model TBABS∗(RELXILLLPCP+GAUSSIAN), in which RELXILLLPCP (García et al. 2013) describes the reflection component plus the hard emission and GAUSSIAN describes the narrow Fe emission line on top of the broad line in RELXILLLPCP. We add their result to Figure 5 as red points, in which we have offset the values by 0.15 for the purpose of display. Their power-law index values are smaller than ours, which is likely due to the differences of the energy bands and the models applied by them and us. However, the overall trends of the evolution of the photon index in their and our work are consistent.

4. Discussion

We have studied the BHC MAXI J1820 the hard state of the 2018 outburst with Insight-HXMT and NICER observations. By analyzing the variability in time and Fourier-domain, we found clear evidence of a transition occurring in this phase: the evolution of the hardness ratio, the fractional rms amplitude and the high-frequency time lag changed from epoch 1 to epoch 2. Additionally, we found that the high-frequency time

lags are correlated with the photon index of the hard component in the energy spectrum.

4.1. Hard-to-hard Spectral State Transition

During the first decay of the 2018 outburst of MAXI J1820, we have observed a hard-to-hard transition, which occurred at around MJD 58,257, when we see the changes in the behavior of the hardness ratio, the fractional rms amplitude and the high-frequency time lags. Since both the hard and soft intensities decrease in this period, it appeared as if the source never entered into a soft state, we suppose that the source went through a failed outburst. By observing the changes of the light curve and the frequency of the low-frequency QPOs in MAXI J1820 with the Swift/XRT and NICER data, Stiele & Kong (2020) also suggested that this source underwent a failed outburst.

A failed outburst is defined as one that either never leaves the hard state, or proceeds to an intermediate state, before returning to the hard state and quiescence during the outburst. A number of cases suggest that the lack of soft-state transitions is possibly associated with a premature decrease of the mass accretion rate, as during the 2008 outburst of H 1743–322 (Capitanio et al. 2009). On the other hand, Del Santo et al. (2016) reported a failed outburst occurring in the BH transient Swift J1745–26 with the source brightness up to $0.4\,L_{\rm EDD}$, implying that a low luminosity is not the sole criterion for such a phenomenon. Adopting a distance to the source of 3 kpc (Atri et al. 2019), a BH mass of $9\,M_\odot$ (Atri et al. 2019) and the maximum unabsorbed flux of $4 \times 10^{-8}\,{\rm erg\,s^{-1}\,cm^{-2}}$ from the fit to the NICER spectrum in the 1–10 keV band, the peak luminosity of MAXI J1820 in our work is around $0.04\,L_{\rm EDD}$, inconsistent with the case reported by Del Santo et al. (2016).

To further investigate this failed outburst in MAXI J1820, we conducted spectral analysis using NICER data between MJD 58,198. The changes in the disk temperature and the photon index between epochs 1 and 2 indicate that the source first softened and then hardened. It is worth noting that the inner disk radius decreased as the disk temperature increased in epoch 1 whereas the inner disk radius remained constant while the disk temperature decreased in epoch 2; the inner disk radius in epoch 2 is smaller overall than that in epoch 1. These changes suggest that the accretion disk moves inwards even when the spectrum is dominated by the hard component, and it stops at a position much larger than the innermost stable circular orbit (adopting a mass of the BH from Atri et al. (2019), $M = 9\,M_\odot$, assuming $R_{\rm ISCO} = 6\,R_{\rm g} = 6\,GM/c^2$, $R_{\rm ISCO} = 79.7$ km). In addition, the changes of the disk temperature and the inner disk radius in epoch 2 are inconsistent with the prediction of the standard accretion disk model, implying that some other physical process(es) leading to these changes is(are) yet to be known.

Both Kara et al. (2019) and Buisson et al. (2019) suggest that the inner part of the accretion disk in MAXI J1820 did not evolve in the hard state of this outburst. However, if we only look into the period of epoch 1, the inner radius of the accretion disk measured by Buisson et al. (2019) decreases with time as well, which is consistent with our result. However, the best-fitting disk inner radius, also the photon index reported here is larger than that in, for instance, Buisson et al. (2019) and B. You et al. (2020, in preparation) and thus the absolute values of the spectral parameters reported in this work should be taken carefully.

4.2. High-frequency Time Lags Associated with Photon Index

We studied the frequency-dependent time lags between the soft, 1–5 keV, and the hard energy bands, up to 150 keV. The low-frequency lags show both/either soft and/or hard lag in one observation, and appear to be independent of energy even though the lag between the 1–5 and the 80–150 keV is larger on average than the ones between the other energy bands. The high-frequency lags, however, show clear evolution along the outburst: they first increase along the outburst in epoch 1 and then decrease in epoch 2, and they are energy-dependent, with the magnitudes of the lags increasing energy (see Figure 4).

Figure 5 shows that the spectra in both epochs are dominated by the hard emission, and that the DISKBB flux only contributes 4%–6% to the total flux in the 1–10 keV band. As shown in Figure 6, the evolution of the high-frequency lags is highly correlated to that of the photon index of the hard spectral component, hinting that the lags are associated with the Comptonized component. The observed high-frequency time lags are thus largely produced by the hard photons, i.e., the high-frequency time lags mainly take place in the Comptonizing region.

Miyamoto et al. (1988) observed a period-dependent time-lag behavior in Cyg X-1, and they proposed that such a phenomenon is due to a perturbing wave traveling from a low-energy- to a high-energy-X-ray-emitting region in the accretion disk and the time delay corresponds to the wave travel-time. Cabanac et al. (2010) further proposed that the broadband noise and low-frequency QPO in the power spectrum could be produced by a magnetoacoustic wave propagating within the corona. Following Equation (1) in Cabanac et al. (2010), the speed of the sound wave is $c_{\rm s} \simeq 3.1 \times 10^8 \left(\frac{T_0}{100\,{\rm keV}}\right)^{1/2}$ cm s^{-1}, proportional to the square root of the electron temperature of the corona. Although the energy band of the NICER data does not allow us to constrain the coronal temperature in MAXI J1820, Buisson et al. (2019) shows that the electron temperature in the corona in MAXI J1820 is proportional to the photon index during the period used in this work. Moreover, Kara et al. (2019) demonstrated that the corona in MAXI J1820 shrinks vertically in epoch 1. The combination of these two facts, increasing sound speed and decreasing path, would lead to a decreasing time lag in this period. Our observations show the opposite behavior. This rules out the possibility that the high-frequency time lag in MAXI J1820 is only caused by a sound wave traveling within the corona.

Another potential model to explain this phenomenon is the inverse Comptonization of soft photons by energetic electrons in a jet (Reig et al. 2018). In their model, when the optical depth/electron density is high, the soft photons are inversely Comptonized by the energetic electrons in the base of the jet. Because of the short mean free path, hard photons are scattered on a short length-scale and hence the corresponding time lag between soft and hard photons is small. As the optical depth decreases, the mean free path increases, leading to a longer time lag and a softer spectrum. In sum, the average time lag of the hard photons with respect to the soft ones increases as the X-ray emission becomes softer. Steady compact radio jets in the hard state of MAXI J1820 have been confirmed by Atri et al. (2019), supporting the model proposed by Reig et al. (2018) as a possible explanation of the high-frequency time lags observed in MAXI J1820. However, the observed time lags are actually smaller than the ones reported by Reig et al. (2018) in similar energy bands. In particular, it may be difficult for this model to produce the factor of ~10 larger lags in the

1–10 Hz frequency range when the hard photon energy increases from several keV to about 100 keV.

A reverberation lag occurs when some of the coronal photons irradiating the accretion disk get reflected and lag behind the primary photons (see a review of the reverberation lag in Uttley et al. 2014). The reverberation lag is thus soft and can constrain the distance between the hard emission region and the accretion disk. Kara et al. (2019) observed a few millisecond reverberation lag between the 0.5–1 and 1–10 keV bands decreasing with time while the accretion disk remains unchanged in MAXI J1820, and they suggested that the corona contracts in this period. Compared to their result, the 1–10 Hz time lags observed in this work are hard and much larger. Although, as a result of the inverse Comptonization in a jet, such lags indicate a large emission region, up to 1000 R_g, this is different from the distance of about $\sim 10\,R_g$ between the accretion disk and the compact corona reported by Kara et al. (2019). However, by jointly fitting the observed motion of the jets in radio and X-rays, Espinasse et al. (2020) obtained an ejection date of the mater in the jets at around MJD 58,305, in which the jet size is very large, i.e., 1.5×10^4 au by 7.7×10^3 au. This result is consistent with a jet of a scale of 1000 R_g in earlier observations. Overall, the results in Kara et al. (2019) and our work suggest that there are two hard emission regions during the studied period of the outburst in MAXI J1820: one is a compact corona and another one is a jet with a large scale.

For the low-frequency time lags, the timescale, dozens of seconds, is more comparable to the time lag predicted by the models of Kotov et al. (2001) and Arévalo & Uttley (2006). They explain the lags as the result of viscous propagation of mass accretion fluctuations within the inner regions of the disk.
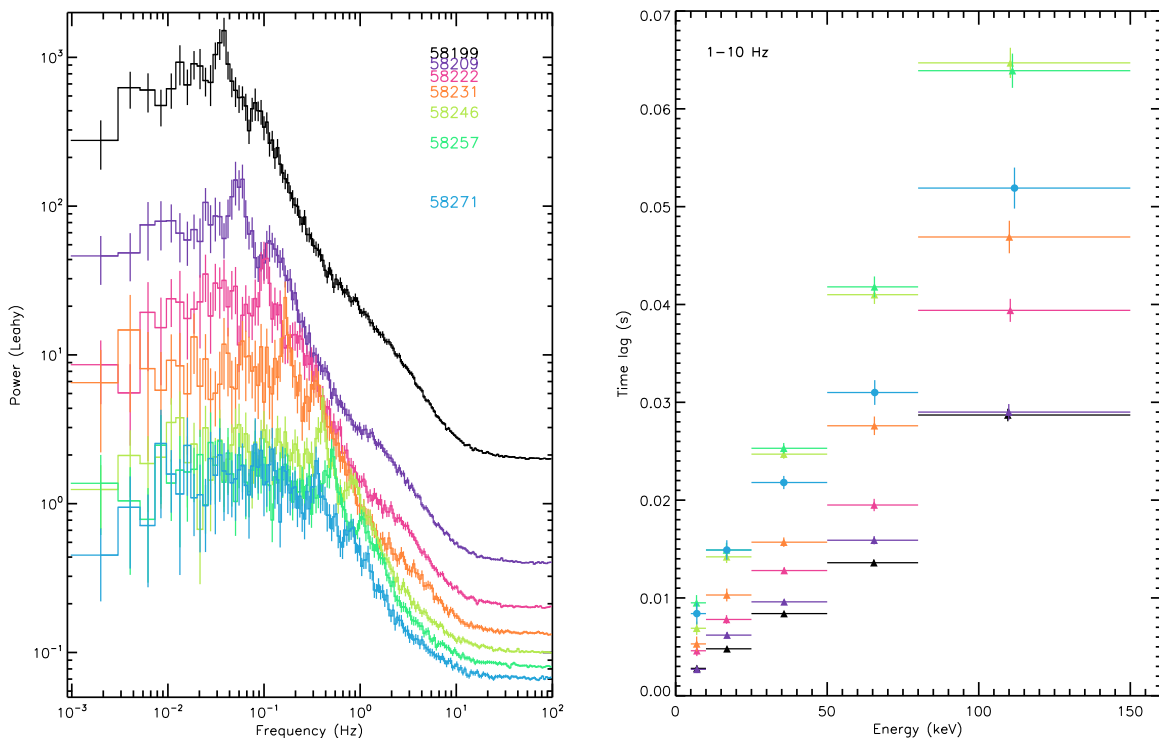
5. Conclusion

We study the evolution of the temporal and spectral properties of MAXI J1820 in its luminous hard state with Insight-HXMT and NICER and find that (1) a hard-to-hard transition occurred at around MJD 58,257, making MAXI J1820 a new case of a transient displaying a failed outburst; (2) the broadband fractional rms amplitude and time lags are all frequency-, flux-, and energy-dependent; (3) the 1–10 Hz time lags are correlated with the photon index of the hard spectral component, qualitatively supporting the model of the lags as caused by Comptonization in a jet.

Appendix

Figure A1 illustrates power spectra and the corresponding time lags in MAXI J1820.

Figure A1. Left: power spectra in MAXI J1820. Except for the PDS at 58199, the following ones have been rescaled by multiplying factors of 0.2, 0.1, 0.067, 0.05, 0.033 and 0.029, respectively, for the purpose of display. The legend on the top right of the panel indicates the observation time of each PDS in MJD. Right: the 1–10 Hz time lags of the shown energy bands with respect to the 1–5 keV band, corresponding to the power spectra in the left panel. The triangles and circle correspond to epochs 1 and 2, respectively.

ORCID iDs

Long Ji ⬤ https://orcid.org/0000-0001-9599-7285
Erlin Qiao ⬤ https://orcid.org/0000-0001-8319-6034

References

Altamirano, D., Belloni, T., Linares, M., et al. 2011, ApJL, 742, L17
Altamirano, D., & Méndez, M. 2015, MNRAS, 449, 4027
Arévalo, P., & Uttley, P. 2006, MNRAS, 367, 801
Atri, P., Miller-Jones, J. C. A., Bahramian, A., et al. 2019, MNRAS, 493, 81
Belloni, T., Klein-Wolt, M., Méndez, M., van der Klis, M., & van Paradijs, J. 2000, A&A, 355, 271
Buisson, D. J. K., Fabian, A. C., Barret, D., et al. 2019, MNRAS, 490, 1350
Cabanac, C., Henri, G., Petrucci, P. O., et al. 2010, MNRAS, 404, 738
Cao, X., Jiang, W., Meng, B., et al. 2020, SCPMA, 63, 249504
Capitanio, F., Belloni, T., Del Santo, M., & Ubertini, P. 2009, MNRAS, 398, 1194
Casella, P., Belloni, T., & Stella, L. 2005, ApJ, 629, 403
Chen, Y., Cui, W., Li, W., et al. 2020, SCPMA, 63, 249505
Chen, Y. P., Zhang, S., Qu, J. L., et al. 2018, ApJL, 864, L30
Del Santo, M., Belloni, T. M., Tomsick, J. A., et al. 2016, MNRAS, 456, 3585
Espinasse, M., Corbel, S., Kaaret, P., et al. 2020, arXiv:2004.06416
Gandhi, P., Paice, J. A., Littlefair, S. P., et al. 2018, ATel, 11437, 1
García, J., Dauser, T., Reynolds, C. S., et al. 2013, ApJ, 768, 146
Grinberg, V., Pottschmidt, K., Böck, M., et al. 2014, A&A, 565, A1
Guo, C.-C., Liao, J.-Y., Zhang, S., et al. 2020, arXiv:2003.06260
Harrison, F. A., Craig, W. W., Christensen, F. E., et al. 2013, ApJ, 770, 103
Huang, Y., Qu, J. L., Zhang, S. N., et al. 2018, ApJ, 866, 122
Huppenkothen, D., Bachetti, M., Stevens, A. L., et al. 2019, ApJ, 881, 39
Kajava, J. J. E., Motta, S. E., Sanna, A., et al. 2019, arXiv:1906.06519
Kara, E., Steiner, J. F., Fabian, A. C., et al. 2019, Natur, 565, 198
Kotov, O., Churazov, E., & Gilfanov, M. 2001, MNRAS, 327, 799
Kuulkers, E., Wijnands, R., Belloni, T., et al. 1998, ApJ, 494, 753
Liao, J.-Y., Zhang, S., Chen, Y., et al. 2020, arXiv:2004.01432
Liu, C., Zhang, Y., Li, X., et al. 2020, SCPMA, 63, 249503
Ludlam, R. M., Miller, J. M., Arzoumanian, Z., et al. 2018, ApJL, 858, L5
Matsuoka, M., Kawasaki, K., Ueno, S., et al. 2009, PASJ, 61, 999
Méndez, M., & van der Klis, M. 1997, ApJ, 479, 926
Méndez, M., van der Klis, M., van Paradijs, J., et al. 1997, ApJL, 485, L37
Miyamoto, S., Kitamoto, S., Mitsuda, K., & Dotani, T. 1988, Natur, 336, 450
Motta, S. E., Casella, P., Henze, M., et al. 2015, MNRAS, 447, 2059
Nowak, M. A., Vaughan, B. A., Wilms, J., Dove, J. B., & Begelman, M. C. 1999, ApJ, 510, 874
Nowak, M. A., Wilms, J., & Dove, J. B. 2002, MNRAS, 332, 856
Pottschmidt, K., Wilms, J., Nowak, M. A., et al. 2003, A&A, 407, 1039
Reig, P., Kylafis, N. D., Papadakis, I. E., & Costado, M. T. 2018, MNRAS, 473, 4644
Remillard, R. A., & McClintock, J. E. 2006, ARA&A, 44, 49
Shidatsu, M., Nakahira, S., Murata, K. L., et al. 2019, ApJ, 874, 183
Soleri, P., Muñoz-Darias, T., Motta, S., et al. 2013, MNRAS, 429, 1244
Stiele, H., & Kong, A. K. H. 2020, ApJ , 889, 142
Takizawa, M., Dotani, T., Mitsuda, K., et al. 1997, ApJ, 489, 272
Tanaka, Y., & Lewin, W. H. G. 1995, in X-ray Binaries, ed. W. H. J. Lewin, J. van Paradijs, & E. P .J. van den Heuvel (Cambridge: Cambridge Univ. Press), 126
Torres, M. A. P., Casares, J., Jiménez-Ibarra, F., et al. 2019, ApJL, 882, L21
Uttley, P., Cackett, E. M., Fabian, A. C., Kara, E., & Wilkins, D. R. 2014, A&ARv, 22, 72
van der Klis, M. 1989, ARA&A, 27, 517
van der Klis, M. 1995, in X-ray Binaries, ed. W. H. G. Lewin, J. van Paradijs, & E. P. J. van den Heuvel (Cambridge: Cambridge Univ. Press), 252
Verner, D. A., Ferland, G. J., Korista, K. T., & Yakovlev, D. G. 1996, ApJ, 465, 487
Wilms, J., Allen, A., & McCray, R. 2000, ApJ, 542, 914
Zhang, L., Wang, Y., Méndez, M., et al. 2017, ApJ, 845, 143
Zhang, S.-N., Li, T., Lu, F., et al. 2020, SCPMA, 63, 249502
Zhou, J. N., Liu, Q. Z., Chen, Y. P., et al. 2013, MNRAS, 431, 2285